Composites Science and Technology xxx (2010) xxx–xxx

Contents lists available at ScienceDirect

Composites Science and Technology

journal homepage: www.elsevier.com/locate/compscitech

Compression-after-impact response of woven fiber-reinforced composites

Hao Yan, Caglar Oskay *, Arun Krishnan, Luoyu Roy Xu

Department of Civil and Environmental Engineering, Vanderbilt University, Nashville, TN 37235, USA

ARTICLE INFO

Article history:
Received 12 April 2010
Received in revised form 23 July 2010
Accepted 17 August 2010
Available online xxxx

Keywords:
B. Delamination
C. Multiscale modeling
C. Damage mechanics
C. Finite element analysis
Compression-after-impact

ABSTRACT

This manuscript investigates compression-after-impact failure in woven fiber-reinforced composites. Compression failure of composite structures previously damaged by an impact event is due to the propagation of impact-induced damage mechanisms such as interlaminar debonding, constituent (i.e., matrix and fiber) microcracking, sublaminate buckling, as well as the interactions between these mechanisms. The failure mechanisms within each ply are idealized based on a reduced order multiscale computational model, in which, the damage propagation in the matrix and fibers upon compression is explicitly modeled. Delamination along the ply interfaces is idealized using a cohesive surface model. The initial impact-induced damage within the microconstituents and interfaces are inferred from experimental observations. A suite of numerical simulations is conducted to understand the sublaminate buckling, propagation of delamination and constituent damage upon compression loading. The numerical investigations suggest extensive propagation of delamination with mode transition preceding sublaminate buckling. Initiation and propagation of matrix and fiber cracking, observed upon sublaminate buckling, is the cause of ultimate shear failure.

© 2010 Elsevier Ltd. All rights reserved.

1. Introduction

Fiber-reinforced composites have been gaining prominence as high performance structural materials in aerospace, naval and automotive industries due to their high specific strength and stiffness. One of the main difficulties with fiber-reinforced composite structures is that their performance degrades once subjected to impact of even modest magnitudes. It is well known that the compressive strength reduces after an impact event, such as tool drop, runway debris impact, bird strikes, and ballistic projectiles in the case of aerospace structures. The impact event typically causes matrix cracking, fiber breakage and delamination within the structure. Under compressive loads, these failure mechanisms interact and the impact-induced damage propagates to failure at significantly lower load levels compared to the undamaged state [1,2].

Considerable research has been devoted to the experimental analysis of compression-after-impact (CAI) behavior of fiber-reinforced composites (e.g., [3–9] among many others). The main foci of the experimental investigations have been (1) characterization of damage within the material due to impact and (2) phenomenological correlation of the reduction in the compressive strength to the impact-induced damage. The primary triggering mechanism of failure in impacted composites is the buckling of sublaminates formed due to the impact event [10]. Impact-induced delamination occurs at a roughly circular region around the impact site. The delaminated region cause local buckling of the sublaminates under compressive loads. The size of the delaminated zone increases with the energy of the impact event, reducing the CAI strength of the material [5,8,9,11]. In addition to the sublaminate buckling, CAI strength may be affected by additional impact-induced damage mechanisms including, distinct matrix cracks at the impact surface, matrix and fiber microcracking, as well as weakening of the interlaminar cohesive strength beyond the delamination zones. Systematic studies of the interactive effects of these damage processes have been relatively scarce. The CAI performance of composites is also significantly affected by the microstructural configuration [9], the mechanical properties of the constituent materials, particularly the resin [11], stacking sequence [12,13] and specimen thickness [2,14,7].

A number of analytical approaches have been proposed for the prediction of CAI strength (e.g., [15–18] among others). Chai et al. [15] employed a fracture mechanics criterion to model the stable and unstable delamination growth in laminated composites. Soutis and coworkers [17] observed the similarity between the failure patterns in laminated composites with an open-hole and impact-damaged composites, and employed a fracture toughness model, originally proposed for open-hole geometry, to predict the CAI strength. Xiong et al. [16] proposed a multistep analytical prediction method, in which the impact damage is modeled as an elliptical soft inclusion. In addition to analytical methods a number of numerical investigations have been conducted to predict the

* Corresponding author. Address: VU Station B#351831, 2301 Vanderbilt Place, Nashville, TN 37235, USA.
E-mail address: caglar.oskay@vanderbilt.edu (C. Oskay).

0266-3538/$ - see front matter © 2010 Elsevier Ltd. All rights reserved.
doi:10.1016/j.compscitech.2010.08.012

buckling load and CAI strength (e.g., [19–21], among others). While the prediction strategies have been relatively successful in estimating the CAI strength, devising preventive strategies against strength degradation requires detailed analysis of failure in the pre- and post-buckling loading regimes, in which all dominant failure mechanisms and their interactions are taken into account [22].

In this manuscript, we conduct a detailed numerical analysis of the compression-after-impact response of a woven fiber composite composed of E-glass fibers and vinyl ester resin. Failure mechanisms of matrix cracking and fiber breakage are explicitly modeled based on a multiscale computational method recently proposed by Oskay and coworkers [23,24]. The propagation of impact-induced delamination at multiple ply interfaces is idealized using a cohesive surface model. The impact-induced damage is incorporated by considering the presence of an initial matrix crack, presence of initial delamination with circular geometry between plies, as well as initial damage along the ply interface outside the delaminated zone. Simulations of a composite specimen subjected to compression-after-impact loading is compared to experimental results. The failure progression along the ply interfaces as well as within the composite constituents is analyzed to identify the failure patterns under compressive loading.

2. CAI experiments

Glass fiber-reinforced vinyl ester (glass/VE) panels were produced using vacuum assisted resin transfer molding (VARTM) process [25]. Eight layers of plain weave glass fabric (CWR 2400/50 plain weave, Composites One, LLC) were used to produce the panels with 4.95 ± 0.1 mm thickness as required by ASTM D 7137 specification. The fiber fraction of the panels was found to be 54 vol. percent after burn off testing was conducted. Compression-after-impact (CAI) testing samples with dimensions 101.6 ± 0.1 mm × 152.4 ± 0.1 mm (4″ × 6″ ± 0.004) were cut and machined to meet the strict dimension requirement specified in ASTM D 7137.

Impact damage was introduced using a drop tower setup [26]. All samples were subjected to an impact with 60 J impact energy using a 16 mm (5/8″) diameter hemisphere impactor. Damage zones of the impacted samples are clearly seen in Fig. 1a and c (at the front and back faces). For the front surface directly subjected to impact, light areas represent internal delamination, with possible several delaminations at the different interfaces. Delaminations were nearly circular in shape with largest radius of 17.6 mm ± 1 mm observed between the back plies. A horizontal and a vertical major matrix crack with dimensions 35.8 and 35.1 ± 2 mm, respectively, was observed near the impact site as shown in Fig. 1a. Immediately behind the drop weight impact site, fiber breakage was observed and this failure mode contributed to impact energy absorption (Fig. 1c). Significant kink banding was not observed in the experiments.

Impacted samples were then mounted into the compression fixture and subjected to compression loading based on ASTM D 7137 specification at the rate of 1 mm/min. Strain gages were attached on the sample back and front surfaces to monitor the strain variations at both surfaces during compression. The reason to use strain monitoring is to avoid any global laminate buckling during compression. The progressive compression failure started from the impact damage site as shown in Fig. 1. Initially, as the compression load increased, impact-induced delamination progressively propagates. The final failure was controlled by sudden extension of the horizontal matrix crack toward the edges of the specimen, as shown in Fig. 1b and d, in addition to the formation of a shear crack through the thickness as shown in Fig. 2. The shear crack was inclined at an angle of 30°–45° with respect to the compressive loading direction. No significant kink band formation was observed within the shear failure zone.

3. Numerical modeling of CAI failure

The geometry, discretization, boundary conditions and impact-induced damage considered in the numerical investigations are illustrated in Fig. 3. A 101.6 × 152.4 cm rectangular plate with 5 mm thickness is modeled. The thickness direction displacement is constrained ($u_3 = 0$) along the edges of the front and back side of the plate, as prescribed by the compression-after-impact test fixture. The compression loading is imparted on the specimen by prescribing vertical displacement at the top surface. The bottom surface of the specimen is restrained in the vertical direction. In the numerical simulations, the prescribed vertical displacements are imposed by considering Dirichlet type boundary condition: $u^2 = \tilde{u}(t)$. $\tilde{u}(t)$ is the prescribed displacement history of the boundary, which is taken to be linearly increasing at the top surface of the specimen and homogeneous at the bottom surface of the specimen. The compressive loading of the specimen mimics the loading in the experimental investigations.

3.1. Impact-induced damage

Four mechanisms of impact-induced damage are considered: (1) the presence of a matrix crack along the fill (horizontal)

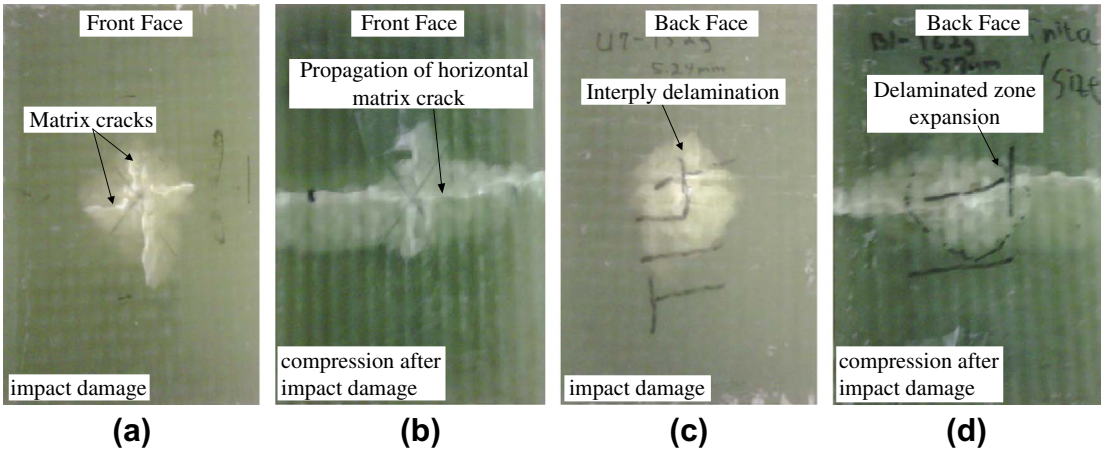

Fig. 1. Damage profiles: (a) impact-induced damage profile viewed from the front (impacted) face, (b) damage profile after compression loading viewed from the front face, (c) Impact-induced damage profile viewed from the back face, and (d) damage profile after compression loading viewed from the back face.

Please cite this article in press as: Yan H et al. Compression-after-impact response of woven fiber-reinforced composites. Compos Sci Technol (2010), doi:10.1016/j.compscitech.2010.08.012

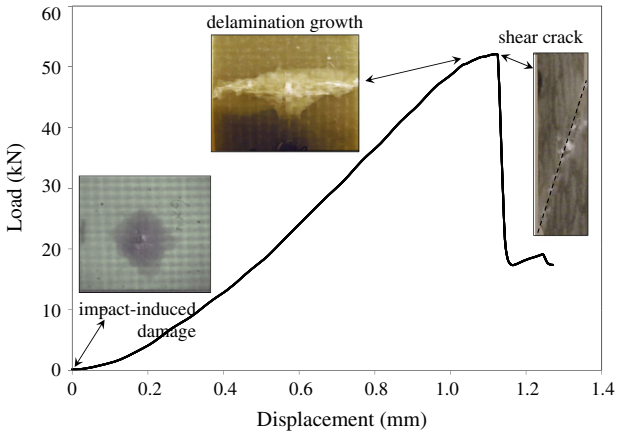

Fig. 2. A schematic of the load-displacement curve of an impacted composite laminate in compression.

direction, (2) delamination within the impact damage zone, (3) loss of strength and cohesive energy along the ply interfaces outside the delaminated zone, and (4) matrix and fiber cracking within the impact damage zone. The experimental results clearly display the presence of two impact-induced matrix cracks along the fill and warp (vertical) directions on the impacted (front) face as shown in Fig. 1a. The experimental investigations suggest that the matrix crack along the fill direction grows, whereas the crack along the warp direction remains unaltered upon compression. Hence, the warp direction matrix crack is not incorporated into the numerical model. The crack orientation and the depth are 45° and one ply length (0.625 mm), respectively. The surface roughness and friction on the faces of the impact-induced matrix crack is assumed to have little effect on the compression response and neglected.

The area of the impact-induced delamination within the sublaminate is assumed to be circular in shape. While the actual measured shape of the delamination zone is typically more complex [13], the assumption of circular delamination zone has been employed in prior investigations [17,27] and adopted in this study. The largest delamination under impact loading is observed between the 7th and 8th plies. It is assumed that the size of the delamination zone between plies increases as a function of thickness [5] as illustrated in Fig. 3b. Delamination is considered between plies 4–5, 5–6, 6–7, and 7–8 only. The areas of delamination between plies 1–2, 2–3, and 3–4 are small and does not significantly affect the CAI response as verified by numerical simulations. Within the zones of impact-induced delamination, interfacial tractions vanish under tensile and shear loading. Friction between the debonded surfaces is ignored. Delaminated plies are prevented from overlapping by employing contact formulation at the zones of delamination. Impact event affects the interlaminar cohesive strength outside the zone of delamination. The cohesive strength as well as the critical energy release rate of the interfaces are found to be smaller than the cohesive strength and the critical energy release rate of the undamaged material. This effect is further discussed in Section 4.

In addition to delamination, the composite constituents undergo damage during the impact event within the area delimited by the cone shape illustrated in Fig. 3b. Some prior investigations considered a complete lack of load carrying capacity of the plies within the damaged area [16,17]. In view of these investigations, we consider that the plies 5–8 have negligible residual strength within the conical damage zone after the impact event.

3.2. Ply failure

Failure mechanisms within each ply are modeled using an eigendeformation-based reduced order computational homogenization (EHM) model recently proposed by Oskay and coworkers [23,24]. The aim and the main contribution of the current investigations are to employ the EHM model to understand failure mechanisms under compression-after-impact loading. In the current modeling approach, the response at the scale of the microstructure is numerically evaluated using simulations conducted on the domain of the representative volume element (RVE). The EHM model employs the transformation field theory [28], which is based on the idea of precomputing certain information about the micro-

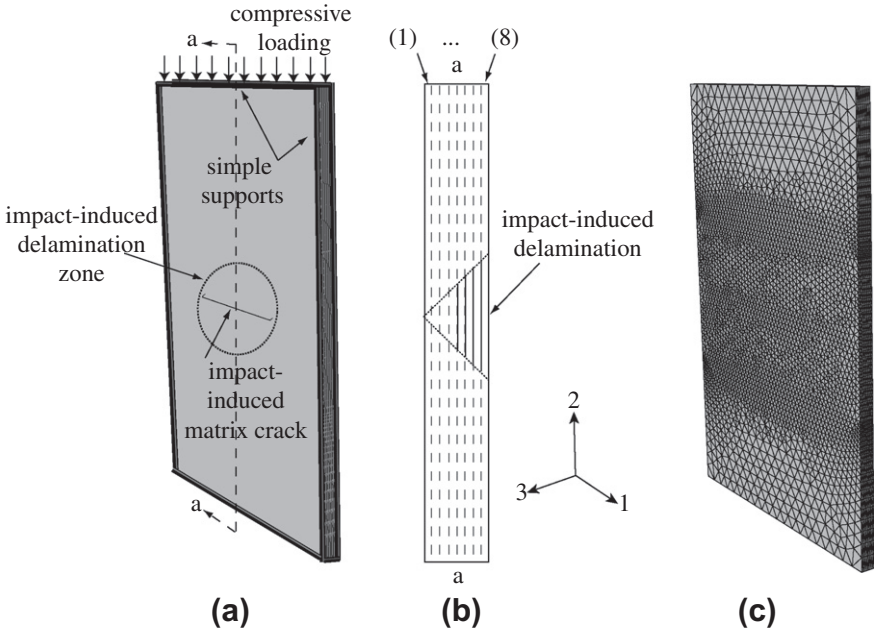

Fig. 3. The numerical model of the CAI specimen: (a) boundary conditions and impact-induced damage, (b) impact-induced delamination along the thickness direction, and (c) finite element discretization of the CAI specimen.

Please cite this article in press as: Yan H et al. Compression-after-impact response of woven fiber-reinforced composites. Compos Sci Technol (2010), doi:10.1016/j.compscitech.2010.08.012

structure of the material (e.g., localization operators, concentration tensors, influence functions) by evaluating linear-elastic RVE scale simulations, prior to the analysis of the macroscale structure. In this approach, the model order is reduced by considering the inelastic response fields to be piecewise constant (in space), within partitions of the RVE. The details of the model is presented in [24] and skipped in this discussion.

The representative volume of the woven composite material is shown in Fig. 4a. The size of the RVE is 10 mm × 12.5 mm × 0.625 mm along the 1–3 directions, respectively. The RVE consists of three constituents: the vinyl ester matrix, fibers along the fill direction, and fibers along the warp direction. Let $\omega_{\mathrm{ph}}^{(\gamma)}$ be a scalar variable indicating the state of damage within constituent γ. $\gamma = m, f, w$ respectively denote the matrix, fibers along the fill and warp directions.

$$\omega_{\mathrm{ph}}^{(\gamma)}(\mathbf{x},t) = \Phi_{\mathrm{ph}}\left(\kappa_{\mathrm{ph}}^{(\gamma)}(\mathbf{x},t)\right); \frac{\partial \Phi_{\mathrm{ph}}\left(\kappa_{\mathrm{ph}}^{(\gamma)}\right)}{\partial \kappa_{\mathrm{ph}}^{(\gamma)}} \geqslant 0 \tag{1}$$

in which, $\kappa_{\mathrm{ph}}^{(\gamma)}$ is expressed as:

$$\kappa_{\mathrm{ph}}^{(\gamma)}(\mathbf{x},t) = \max_{\tau \leqslant t}\left(\upsilon_{\mathrm{ph}}^{(\gamma)}(\mathbf{x},\tau)\right) \tag{2}$$

where, $\upsilon_{\mathrm{ph}}^{(\gamma)}$ is phase damage equivalent strain defined based on the strain-based damage theory [29] as:

$$\upsilon_{\mathrm{ph}}^{(\gamma)}(\mathbf{x},t) = \sqrt{\frac{1}{2}\left(\mathbf{F}^{(\gamma)}\hat{\boldsymbol{\epsilon}}^{(\gamma)}\right)^{\mathrm{T}}\hat{\mathbf{L}}^{(\gamma)}\left(\mathbf{F}^{(\gamma)}\hat{\boldsymbol{\epsilon}}^{(\gamma)}\right)} \tag{3}$$

in which, $\hat{\boldsymbol{\epsilon}}^{(\gamma)}$ is the vector of principal components of the average strains, $\epsilon_{ij}^{(\gamma)}$, within constituent phase, γ; $\hat{\mathbf{L}}^{(\gamma)}$ the tensor of elastic moduli in principal directions of $\epsilon_{ij}^{(\gamma)}$, and; $\mathbf{F}^{(\gamma)}$ the weighting matrix. The weighting matrix differentiates between damage accumulation when under tensile and compressive loading

$$\mathbf{F}^{(\gamma)}(\mathbf{x},t) = diag\left(h_1^{(\gamma)}, h_2^{(\gamma)}, h_3^{(\gamma)}\right) \tag{4}$$

$$h_\xi^{(\gamma)}(\mathbf{x},t) = \frac{1}{2} + \frac{1}{\pi}\,\mathrm{atan}\left(c_1^{(\gamma)}\hat{\epsilon}_\xi^{(\gamma)}\right); \zeta = 1,2,3 \tag{5}$$

where $c_1^{(\gamma)}$ represents the contribution of tensile and compressive loadings in the principal directions, and $diag(\cdot)$ denotes diagonal matrix.

The phase damage evolution function follows an arctangent law [30]

$$\Phi_{\mathrm{ph}}^{(\gamma)} = \frac{\mathrm{atan}\left(a_{\mathrm{ph}}^{(\gamma)}\kappa_{\mathrm{ph}}^{(\gamma)}(\mathbf{x},t) - b_{\mathrm{ph}}^{(\gamma)}\right) + \mathrm{atan}\left(b_{\mathrm{ph}}^{(\gamma)}\right)}{\pi/2 + \mathrm{atan}\left(b_{\mathrm{ph}}^{(\gamma)}\right)} \tag{6}$$

in which, $a_{\mathrm{ph}}^{(\gamma)}$ and $b_{\mathrm{ph}}^{(\gamma)}$ are material parameters.

The RVE average (macroscale) stress of the overall woven composite material is expressed in terms of the RVE average (macroscale) strain, $\bar{\epsilon}_{ij}$, and the constituent average of the damage-induced inelastic strains (i.e., eigenstrains) $\mu_{ij}^{(\gamma)}$:

$$\bar{\sigma}_{ij}(\mathbf{x},t) = \bar{L}_{ijkl}\bar{\epsilon}_{kl}(\mathbf{x},t) + \sum_{\gamma}\overline{M}_{ijkl}^{(\gamma)}\mu_{kl}^{(\gamma)}(\mathbf{x},t) \tag{7}$$

The resulting macroscale stress–strain relationship is schematically illustrated in Fig. 5a. $\mu_{ij}^{(\gamma)}$ is obtained by solving the following nonlinear equation:

$$\sum_{\gamma=1}^{n}\left[\delta_{\eta\gamma}^{\mathrm{K}}I_{ijkl} - P_{ijkl}^{(\eta\gamma)}\omega_{\mathrm{ph}}^{(\eta)}(\mathbf{x},t)\right]\mu_{kl}^{(\gamma)}(\mathbf{x},t) = \omega_{\mathrm{ph}}^{(\eta)}(\mathbf{x},t)A_{ijkl}^{(\eta)}\bar{\epsilon}_{kl}(\mathbf{x},t); \eta = m,f,w \tag{8}$$

in which, $\delta_{\gamma\eta}^{\mathrm{K}}$ is the Kronecker delta; I_{ijkl} the fourth order identity tensor; the coefficient tensors, $P_{ijkl}^{(\eta\gamma)}, A_{ijkl}^{(\eta)}$ and $\overline{M}_{ijkl}^{(\gamma)}$ are expressed as:

$$P_{ijkl}^{(\eta\gamma)} = \frac{1}{|\Theta^{(\eta)}|}\int_{\Theta^{(\eta)}}\int_{\Theta^{(\gamma)}} g_{ijkl}^{\mathrm{ph}}(\mathbf{y},\hat{\mathbf{y}})d\hat{y}dy \tag{9}$$

$$A_{ijkl}^{(\eta)} = \frac{1}{|\Theta^{(\eta)}|}\int_{\Theta^{(\eta)}}(I_{ijkl} + G_{ijkl})(\mathbf{y})dy \tag{10}$$

$$\overline{M}_{ijkl}^{(\gamma)} = \frac{1}{|\Theta|}\int_{\Theta}\int_{\Theta^{(\gamma)}} L_{ijmn}(\mathbf{y})g_{ijkl}^{\mathrm{ph}}(\mathbf{y},\hat{\mathbf{y}})d\hat{y}dy - L_{ijkl}^{(\gamma)} \tag{11}$$

where, Θ and $\Theta^{(\eta)}$ denote the domains of the RVE and the domain of the constituent, η, respectively, and; g_{ijkl}^{ph} and G_{ijkl} are the damage-induced and elastic polarization functions computed using the fundamental solutions of the RVE problem based on the EHM method. The fundamental solutions and the polarization functions of the RVE are evaluated numerically [23]. $L_{ijkl}^{(\gamma)}$ denotes the tensor of elastic moduli in constituent, γ.

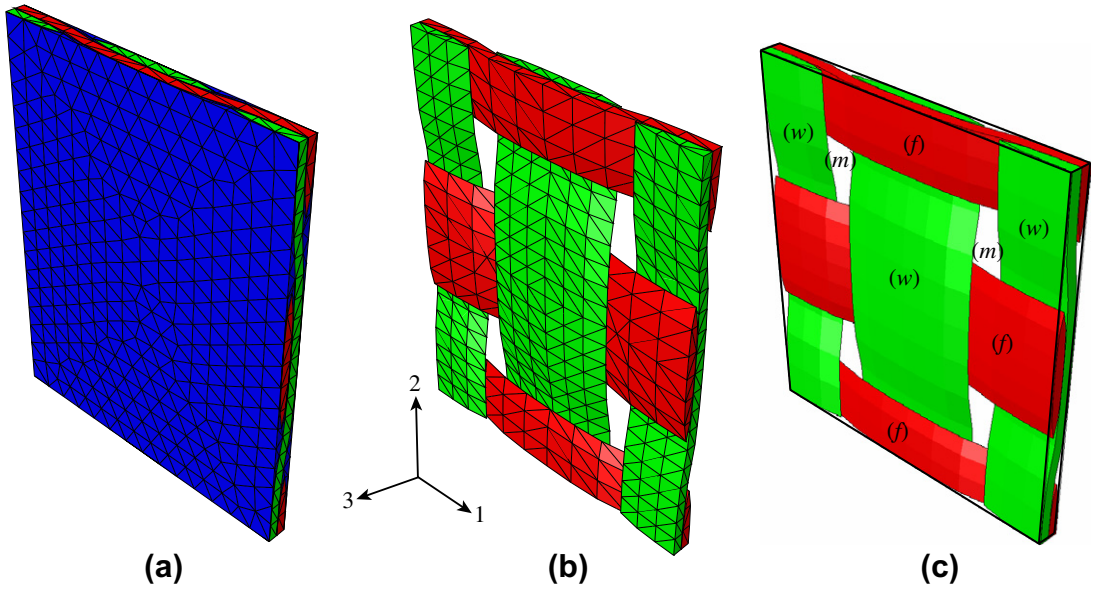

Fig. 4. The representative volume for the woven composite material (a) finite element discretization, (b) finite element discretization of the fibers, and (c) reduced order model for the RVE with three constituents: fill (horizontal) and warp (vertical) fibers and the matrix (transparent).

Please cite this article in press as: Yan H et al. Compression-after-impact response of woven fiber-reinforced composites. Compos Sci Technol (2010), doi:10.1016/j.compscitech.2010.08.012

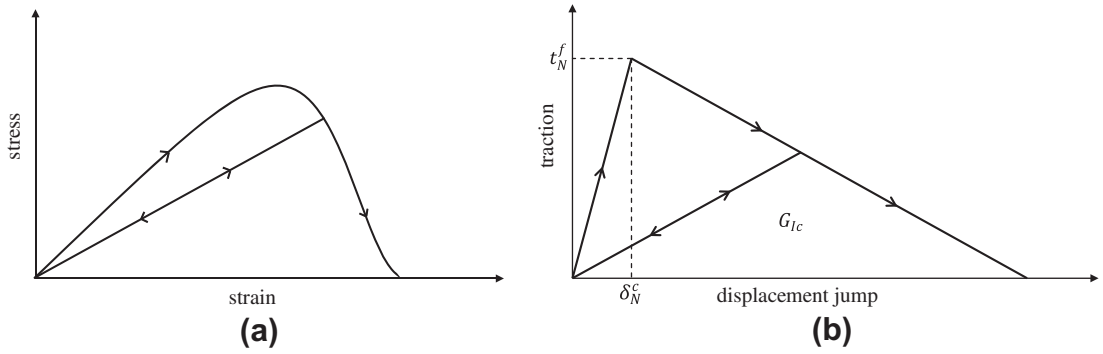

Fig. 5. Illustration of the damage progression models: (a) bilinear cohesive law for delamination propagation in case of pure mode I condition. A mixed mode cohesive surface law is employed in the simulations and (b) damage evolution law for composite constituents.

3.2.1. Calibration of undamaged material parameters

The multiscale model that defines the failure behavior within the plies includes 9 failure parameters: $a_{\mathrm{ph}}^{(\gamma)}$, $b_{\mathrm{ph}}^{(\gamma)}$, $c_1^{(\gamma)}$; $\gamma = m, w, f$. Assuming isotropic behavior for the microconstituents; four elastic constants define the elastic response of the woven composite: $E^{(m)}$, $\nu^{(m)}$, $E^{(w)} = E^{(f)}$, and $\nu^{(w)} = \nu^{(f)}$. $E^{(\gamma)}$ and $\nu^{(\gamma)}$ denote the Young's modulus and Poisson's ratio in constituent γ, respectively.

The experimentally observed and simulated elastic and strength properties of the composite material are summarized in Table 1. Experimentally determined tensile moduli of the matrix and fiber materials are 3.4 GPa [31] and 70 GPa [32], respectively. The tensile stiffness of the composite material along the warp and fill directions are 29.2 GPa and 23.9 GPa, respectively. The stiffness of the composite material under compression along the warp and fill directions are 31.9 GPa and 26.9 GPa. The Poisson's ratios of the composite material along warp and fill directions are 0.14 and 0.16, respectively. In our simulations, we employ the experimentally provided matrix and fiber stiffness values: $E^{(m)} = 3.4$ GPa and $E^{(f)} = 70$ GPa. Experimental measurements of the Poisson's ratios for the constituent materials are not available. We therefore assume that the constituent Poisson's ratios are equal to the average Poisson's ratio of the overall composite (i.e., $\nu^{(m)} = \nu^{(f)} = 0.15$). The composite stiffness properties are evaluated based on the linear-elastic computational homogenization method [33]:

$$\bar{L}_{ijkl} = \frac{1}{|\Theta|}\int_{\Theta} L_{ijmn}(G_{mnkl} + I_{mnkl})d\Theta \tag{12}$$

in which, $\bar{L}_{ijkl}$ denotes the tensor of elastic moduli of the composite. The computed elastic moduli for the overall composite and the experimental values are in good agreement as summarized in Table 1.

Table 1
Stiffness and strength properties of the composite material provided by experiments [31] and RVE scale simulations.

Composite properties	Experiments	Simulations
Compression modulus (GPa)		
Warp direction	31.9	30.5
Fill direction	26.9	25.5
Tension modulus (GPa)		
Warp direction	29.2	30.5
Fill direction	23.9	25.5
Compression strength (MPa)		
Warp direction	363.4 (75.0)[a]	357.0
Fill direction	336.4 (25.2)	353.0
Tension strength (MPa)		
Warp direction	512.5 (22.5)	481.0
Fill direction	350.9 (8.9)	332.0
Poisson's ratio		
Warp direction	0.16 (0.01)	0.15
Fill direction	0.14 (0.003)	0.15

[a] Standard deviation.

The failure parameters $a_{\mathrm{ph}}^{(\gamma)}$ and $b_{\mathrm{ph}}^{(\gamma)}$ define the evolution of damage throughout the loading history, whereas, $c_1^{(\gamma)}$ differentiate between the tensile and compressive failure behavior. The strength of the constituent materials and the overall composite along the tensile and compressive directions provided by the experimental investigations are employed to calibrate the fiber and matrix failure parameters. The calibrated material parameters are summarized in Table 2. The stress–strain response of the overall composite computed by unit cell simulations is shown in Fig. 6. The simulated strength values are in reasonable agreement with the experiments as summarized in Table 1.

3.3. Interlaminar failure

The failure along the interfaces between composite laminates is modeled using cohesive surfaces. To this extent, the traction–displacement relationship along the interlaminar boundaries are expressed as:

$$\mathbf{t} = (1 - \omega_{\mathrm{int}})\mathbf{K}\boldsymbol{\delta} \tag{13}$$

in which, $\mathbf{t} = \{t_N, \mathbf{t}_S\}$ is traction vector with normal and shear components are indicated by subscripts, N and S, respectively; $\mathbf{K} = diag(K_N, K_S, K_S)$the diagonal interface stiffness matrix; $\boldsymbol{\delta} = \{\delta_N, \boldsymbol{\delta}_S\}$, the displacement jump vector, and; ω_{int} is a history dependent variable describing the state of damage. The evolution of damage as a function of displacement jump is schematically described in Fig. 5b. A linear damage evolution law is adopted in this study. The damage growth initiation criteria describes the range of effective displacement jump that corresponds to no accumulation of damage:

$$\lambda_c = \sqrt{\left\{\frac{\langle\delta_N\rangle}{\delta_N^c}\right\}^2 + \left\{\frac{\|\boldsymbol{\delta}_S\|}{\delta_S^c}\right\}^2} \leqslant 1 \tag{14}$$

Hence the damage initiates when λ_c reaches unity. Upon initiation, the evolution of damage is expressed as:

$$\dot{\omega}_{\mathrm{int}} = \frac{\kappa_f \kappa_c}{\kappa^2(\kappa_f - \kappa_c)}\dot{\kappa} \tag{15}$$

in which, $\kappa_c = \sqrt{(\delta_N^c)^2 + (\delta_S^c)^2}$ denotes the critical equivalent displacement jump at the initiation of damage growth, and; κ_f denotes equivalent displacement jump at ultimate debonding

Table 2
Calibrated strength parameter for the composite constituent materials.

$a_{\mathrm{ph}}^{(f)}$	$b_{\mathrm{ph}}^{(f)}$	$c_1^{(f)}$	$a_{\mathrm{ph}}^{(w)}$	$b_{\mathrm{ph}}^{(w)}$	$c_1^{(w)}$	$a_{\mathrm{ph}}^{(m)}$	$b_{\mathrm{ph}}^{(m)}$	$c_1^{(m)}$
1.5	2.3	5.0	1.0	2.0	−28.0	400.0	168.0	0.0

Please cite this article in press as: Yan H et al. Compression-after-impact response of woven fiber-reinforced composites. Compos Sci Technol (2010), doi:10.1016/j.compscitech.2010.08.012

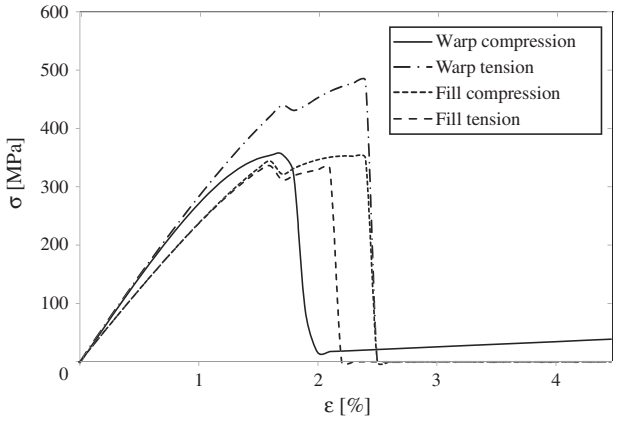

Fig. 6. The stress–strain response of the composite RVE along the fill and warp directions under compressive and tensile loading.

$$\kappa_f = \sqrt{\frac{4G_c^2}{(t_N^f)^2 + \left(t_S^f\right)^2}} \tag{16}$$

where, t_N^f and t_S^f are ultimate normal and shear tractions along the interface, respectively. $\kappa = \max_{\tau \leqslant t} \| \delta(\tau) \|$ is the maximum equivalent displacement jump attained throughout the history of loading. The mixed mode condition for cohesive cracking is modeled using the Benzeggah–Kenane criterion [34]:

$$G_c = G_{Ic} + (G_{IIc} - G_{Ic}) \left[\frac{G_S}{G}\right]^{\eta} \tag{17}$$

in which, η is a material parameter defining mode mixity; G_S/G denotes the fraction of the cohesive energy dissipated by shear tractions, G the work done by the interface tractions; G_S the work done by the shear components of interface tractions, and; G_{Ic} and G_{IIc} are critical mode I and II energy release rates, respectively.

3.3.1. Calibration of undamaged material parameters

The cohesive surface model includes seven independent parameters. The interface stiffness coefficients along the normal and shear directions are related to the equivalent Young's and shear moduli within the interface region: $K_N = E_{eq}/h$ and $K_S = G_{eq}/h$, in which, h is the thickness of the interface region. E_{eq} and G_{eq} are typically bounded by the stiffness of the constituent materials: $E_{matrix} \leqslant E_{eq} \leqslant E_{fiber}$ and $G_{matrix} \leqslant G_{eq} \leqslant G_{fiber}$. In this study, we assume that the equivalent elastic and shear moduli within the interface region are equal to the homogenized moduli of the composite material along the thickness direction: $E_{eq} = \overline{E}_{33}$ and $G_{eq} = \overline{G}_{23} = \overline{G}_{13}$. The orientation of the composite representative volume element is illustrated in Fig. 4. The interface region thickness in our simulations is taken to be 100 μm. The interface thickness is calculated based on the composite RVE, as the average resin thickness between plies.

The ultimate normal and shear tractions along the interface are bounded by the strength of the constituent materials: $\sigma^f_{matrix} \leqslant t^f_N \leqslant \sigma^f_{fiber}$ and $\tau^f_{matrix} \leqslant t^f_S \leqslant \tau^f_{fiber}$. σ^f_{matrix} and σ^f_{fiber} denote the tensile strength of the matrix and fiber materials along the thickness direction, respectively, and; τ^f_{matrix} and τ^f_{fiber} are the shear strength values. In this study, the ultimate normal and shear tractions are taken to be equal to the normal and shear strength of the composite: $t^f_N = \bar{\sigma}^f_{33} = 109.25$ MPa and $t^f_S = \bar{\tau}^f_{23} = \bar{\tau}^f_{13} = 42.5$ MPa. The components of the critical equivalent displacement jump vector are: $\delta^c_N = t^f_N/K_N$ and $\delta^c_S = t^f_S/K_S$. Critical energy release rates for interface delamination in composite systems typically vary between 200-2000 J/m^2 range [35]. The experiments conducted by Ref. [36] reported G_{Ic} and G_{IIc} values of 1210 J/m^2 and 4550 J/m^2, respectively, for a composite configuration similar to that under investigation in this study. These values are taken to be the undamaged material properties in our investigations, acknowledging the significant variations in experimentally reported G_{Ic} and G_{IIc} values for similar materials [35]. The mode mixity parameter, η, is calibrated based on the experimental measurements provided by Dharmawan et al. [36]. $\eta = 1.53$ is the optimal mode mix parameter in the least square sense.

4. Numerical simulation of CAI response

4.1. Sublaminate buckling

A series of simulations have been conducted to estimate the critical compressive loads that lead to local buckling at the impact-induced damage zone. Fig. 7 shows the numerically computed buckling loads for two failure scenarios in impacted specimens compared to the experimental observations and the undamaged material. The constituent materials are assumed to be elastic and delaminated zones are assumed to remain unaltered during the buckling simulations. When the damage within the composite constituents and delaminations are restricted to the impact-induced configuration as described in Section 3.1 – which assumes no significant damage progression prior to buckling – the buckling strength is 173 MPa. The computed value is significantly higher than the failure strength observed in the experiments (117 MPa with standard deviation of 8.6 MPa). This suggests that the theoretical buckling strength of impact-induced damage configuration overestimates the compressive strength. Damage progression during the compression loading event is critical in predicting the CAI failure. When the delamination zone is extended across the specimen within middle third of the specimen – which corresponds to maximum level of delamination prior to buckling – the buckling strength is 103 MPa. The computed buckling strength is slightly lower than the experimental observations, indicating that significant delamination propagation precedes sublaminate buckling under compression loading.

4.2. Delamination propagation

The buckling analysis, as well as the experimental observations indicates propagation of delamination prior to the onset of failure. We investigated delamination propagation along the ply interfaces. The simulations in this section do not consider progression of damage within the composite constituents. Delamination propagation is modeled by introducing cohesive surface models within the middle third of each ply interface outside the initial impact-induced delamination zone. Within the impact-induced delamination zone, zero cohesive strength is considered. Numerical simulations conducted using the undamaged critical energy release rates

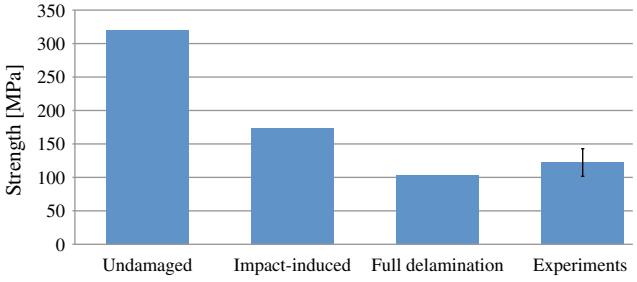

Fig. 7. Experimental and simulated sublaminate buckling strength of composite specimens.

Please cite this article in press as: Yan H et al. Compression-after-impact response of woven fiber-reinforced composites. Compos Sci Technol (2010), doi:10.1016/j.compscitech.2010.08.012

reported in Ref. [36] (G_{Ic} = 1210 J/m^2 and G_{IIc} = 4550 J/m^2) for a similar material configuration, and the undamaged ultimate traction values ($t_N^f = 109.25$ MPa and $t_S^f = 42.5$ MPa) indicated no significant delamination propagation up to the experimentally observed failure load. This is in contrast with our experimental observations, in which, the response is marked by delamination propagation at load levels lower than the ultimate failure. We therefore employed a parameteric analysis to investigate the effect of impact on the strength and critical energy release rate beyond the circular initial delamination zones. Numerical investigations indicate that the delamination propagation is strongly influenced by the loss of interfacial strength, and to a lesser extent, to the reduction in critical energy release rates. Experimentally verified propagation of delamination prior to the onset of sublaminate buckling are observed in the simulations when the critical energy release rates of G_{Ic} = 200 J/m^2 and G_{IIc} = 756 J/m^2, and the ultimate normal and shear strength of 27.3 MPa and 10.6 MPa, respectively, are employed. The critical energy release rates remain to be consistent with, yet slightly lower than the experimentally observed range. The reduced strength and critical energy release rates point to the presence of impact-induced damage beyond the circular delamination zone. In addition, recent investigations [37] based on an efficient short-beam shear approach to measure the mode II fracture toughness of bonded materials and composites indicate that mode-II fracture toughness of undamaged materials is lower than those measured based on previous techniques.

Fig. 8a–c shows the interface damage profiles between 4th and 5th plies during compression loading at loading levels of 29 MPa, 86 MPa, and 138 MPa. At relatively low load level, the delamination propagates above and below the impact-induced delamination zone (Fig. 8a). The propagation is dominated by the component of shear traction along the vertical direction (loading direction). Further compressive loading extends the delamination around the impact-induced delamination zone. The vertical shear dominated zones coalesce and further propagate laterally toward the sides of the specimen. A mode transition is observed during the coalescence of the shear cracks and the lateral delamination propagation is dominated by lateral component of the shear tractions. It has also been observed that the delamination propagation across the middle plies occur at lower load levels compared to the back plies despite smaller impact-induced initial delamination zones (Fig. 8d–f).

4.3. Constituent damage propagation

Matrix and fiber shear cracking is the experimentally observed cause of final failure under compression loading. We investigated the nature of constituent damage propagation through numerical simulations. In these simulations, both delamination propagation and constituent damage propagation mechanisms are considered. Fig. 9 illustrates the damage propagation in the matrix and warp direction fibers. Relatively small damage accumulation is observed within the constituents until loading reaches the critical sublaminate buckling load. At this level, full delamination is observed between 4th and 5th plies, which triggers buckling. Upon buckling, the fiber and matrix crack propagation initiate at the back face of the specimen, propagating laterally towards the side of the specimen and along the thickness direction, in shear mode. The shear crack, which causes ultimate failure within the specimen, is shown in Fig. 9g. The stress–strain diagram of the overall specimen under compression loading is compared to the experiments in Fig. 10. Our simulations provide a good quantitative match with the experimental observations. The compressive strength of the simulated specimen is 116.67 MPa, which is within 0.45% of the average compressive strength observed in the experiments (117.19 MPa). The average strain to failure based on experiments and the simulations are 0.4217% and 0.422%, respectively.

5. Conclusions

This manuscript provided a detailed numerical investigation of the compression-after-impact response of woven E-glass fiber-reinforced vinyl ester composite materials. The numerical investigations are validated against a suite of CAI experiments. We report the following findings: (1) The critical energy release rate to propagate the delamination of impact-induced ply debonds are lower than those observed experimentally in undamaged specimens of similar materials. This indicates impact-induced damage even beyond the cone-shaped initial impact-induced damage zone. (2) Delamination propagation is the critical mechanism that lowers the sublaminate buckling strength of impacted specimens. Delamination propagation extends throughout the width of the specimen between middle plies, which triggers the sublaminate buckling. (3) Delamination propagation is marked by a mode transition: the loading direction shear dominated initial impact-induced delami-

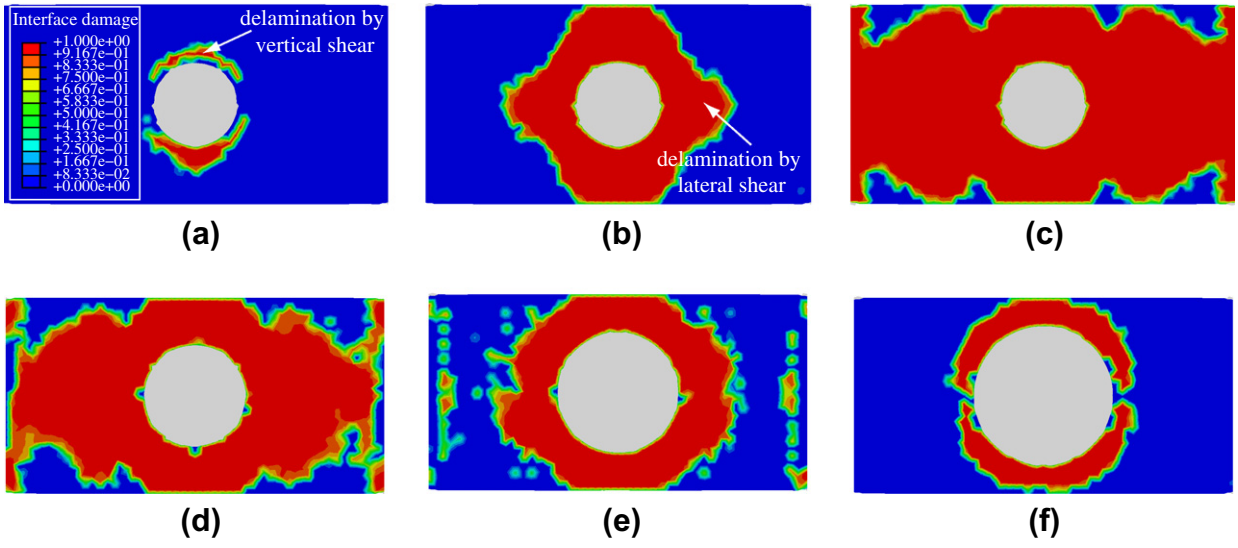

Fig. 8. Interface damage profiles between: (a) 4th and 5th plies under 29 MPa compression, (b) 4th and 5th plies under 86 MPa compression, (c) 4th and 5th plies under 138 MPa compression, (d) 5th and 6th plies under 138 MPa compression, (e) 6th and 7th plies under 138 MPa compression, and (f) 7th and 8th plies under 138 MPa compression.

Please cite this article in press as: Yan H et al. Compression-after-impact response of woven fiber-reinforced composites. Compos Sci Technol (2010), doi:10.1016/j.compscitech.2010.08.012

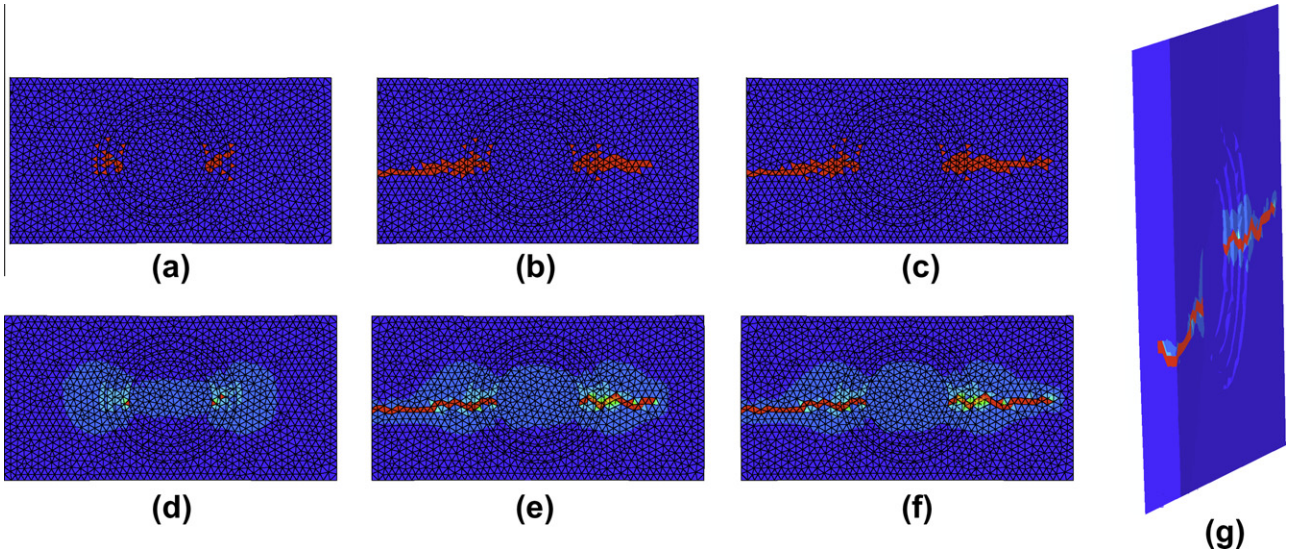

Fig. 9. Damage propagation in the composite constituents upon sublaminate buckling: (a)–(c) propagation of matrix damage, (d)–(f) propagation of warp fiber damage, and (g) shear crack propagation causing ultimate failure. The middle third of the specimen is shown (back face).

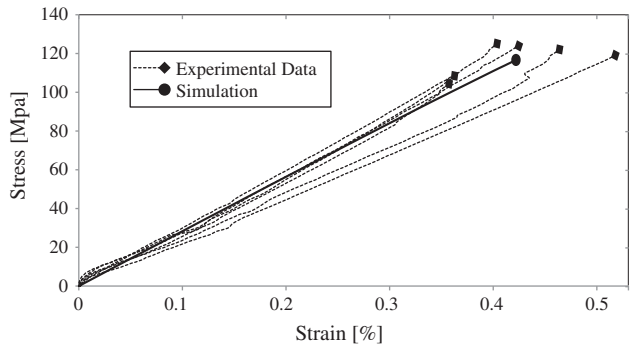

Fig. 10. CAI Stress–strain diagram of the composite specimen based on numerical simulations and experiments.

nation extends in low amplitude compression loads, which transitions to the a lateral shear dominated delamination at higher amplitudes. The delamination then extends laterally toward the sides of the specimen. (4) Significant constituent (matrix and fiber) cracking is observed only upon sublaminate buckling. The constituent cracks initiate at the back face of the specimen. The constituent cracks propagate laterally and along the thickness direction in shear mode to cause the ultimate failure of the specimen under compressive loading.

Acknowledgement

The authors acknowledge the support from the Office of Naval Research and the National Science Foundation. The authors also acknowledge Prof. Uday Vaidya at University of Alabama, Birmingham (UAB) for providing samples and allowing us to conduct experiments at UAB testing facilities.

References

[1] Cantwell WJ, Curtis P, Morton J. An assessment of the impact performance of cfrp reinforced with high-strain carbon fibers. Compos Sci Technol 1986;25:503–11.
[2] Prichard JC, Hogg PJ. The role of impact damage in post-impact compression testing. Composites 1990;21:503–11.
[3] Ishikawa T, Sugimoto S, Matsushima M, Hayashi Y. Some experimental findings in compression-after-impact (CAI) tests of cf/peek (apc-2) and conventional cf/epoxy flat plates. Compos Sci Technol 1995;55:349–63.
[4] Wang H, Chen PH, Shen Z. Experimental studies on compression-after-impact behavior of quasi-isotropic composite laminates. Sci Eng Compos Mater 1997;6:19–35.
[5] de Freitas M, Reis L. Failure mechanisms on composite specimens subjected to compression after impact. Compos Struct 1998;42:365–73.
[6] Hosur MV, Murthy CRL, Ramurthy TS. Compression after impact testing of carbon fiber reinforced plastic laminates. ASTM J Compos Technol Res 1999;21:51–64.
[7] Naik NK, Joglekar MN, Arya H, Borade SV, Ramakrishna KN. Impact and compression after impact characteristics of plain weave fabric composites: effect of plate thickness. Adv Compos Mater 2004;12:261–80.
[8] Sanchu-Saez S, Barbero E, Zaera R, Navarro C. Compression after impact of thin composite laminates. Compos Sci Technol 2005;65:1911–9.
[9] Khondker OA, Leong KH, Herszberg I, Hamada H. Impact and compression-after-impact performance of weft-knitted glass textile composites. Compos Part A: Appl Sci Manuf 2005;36:638–48.
[10] Baker AA, Jones R, Callinan RJ. Damage tolerance of graphite/epoxy composites. Compos Struct 1985;4:15–44.
[11] Cartie DDR, Irving PE. Effect of resin and fibre properties on impact and compression after impact performance of cfrp. Compos Part A: Appl Sci Manuf 2002;33:483–93.
[12] Hong S, Liu D. On the relationship between impact energy and delamination area. Exp Mech 1989;29:115–20.
[13] Hitchen SA, Kemp RMJ. The effect of stacking-sequence on impact damage in carbon–fibre epoxy composite. Composites 1995;26:207–14.
[14] Liu D, Raju BB, Dang XL. Size effects on impact response of composite laminates. Int J Impact Eng 1998;21:837–54.
[15] Chai H, Babcock CD, Knauss WG. One dimensional modelling of failure in laminated plates by delamination buckling. Int J Solids Struct 1981;17:1069–83.
[16] Xiong Y, Poon C. A prediction method for the compressive strength of impact damaged composite laminates. Compos Struct 1995;30:357–67.
[17] Soutis C, Curtis PT. Prediction of the post-impact compressive strength of cfrp laminated composites. Compos Sci Technol 1996;56:677–84.
[18] Khondker OA, Herszberg I, Hamada H. Measurements and prediction of the compression-after-impact strength of glass knitted textile composites. Compos Part A: Appl Sci Manuf 2004;35:145–57.
[19] Chen VL, Wu HYT, Yeh HY. A parametric study of residual strength and stiffness for impact damaged composites. Compos Struct 1993;25:267–75.
[20] Sekine H, Hu N, Kouchakzadeh MA. Buckling analysis of elliptically delaminated composite laminates with consideration of partial closure of delamination. J Compos Mater 2000;34:551–74.
[21] Habib FA. A new method for evaluating the residual compression strength of composites after impact. Compos Struct 2001;53:309–16.
[22] Lee SM, Zahuta P. Instrumented impact and static indentation of composites. J Compos Mater 1991;25:204–22.
[23] Oskay C, Fish J. Eigendeformation-based reduced order homogenization for failure analysis of heterogeneous materials. Comput Methods Appl Mech Eng 2007;196:1216–43.
[24] Crouch R, Oskay C. Symmetric meso-mechanical model for failure analysis of heterogeneous materials, Int J Mult Comp Eng, in press.

Please cite this article in press as: Yan H et al. Compression-after-impact response of woven fiber-reinforced composites. Compos Sci Technol (2010), doi:10.1016/j.compscitech.2010.08.012

[25] Pillay S, Vaidya UK, Janowski GM. Liquid molding of carbon fabric-reinforced nylon matrix composite laminates. J Thermoplast Compos Mater 2005;18:509–27.
[26] Ulven C, Vaidya UK. Post-fire low velocity impact response of marine grade sandwich composites. Compos Part A: Appl Sci Manuf 2006;37:997–1004.
[27] Guynn EG, O'Brien K. The influence of lay-up and thickness on composite impact damage and compression strength. In: Proceedings of 26th structures, structural dynamics, materials conference, Orlando, FL: April 1985. p. 187–96.
[28] Dvorak GJ, Benveniste Y. On transformation strains and uniform fields in multiphase elastic media. Proc Roy Soc Lond A 1992;437:291–310.
[29] Simo JC, Ju JW. Strain- and stress-based continuum damage models. I. Formulation. Int J Solids Struct 1987;23(7):821–40.
[30] Fish J, Yu Q, Shek K. Computational damage mechanics for composite materials based on mathematical homogenization. Int J Numer Methods Eng 1999;45:1657–79.
[31] Tekalur SA, Shivakumar K, Shukla A. Mechanical behavior and damage evolution in e-glass vinyl ester and carbon composites subjected to static and blast loads. Compos Part B: Eng 2008;39:57–65.
[32] Roy R, Sarkar BK, Bose NR. Behavior of e-glass fibre reinforced vinylester resin composites under impact fatigue. Bull Mater Sci 2001;24:137–42.
[33] Guedes JM, Kikuchi N. Preprocessing and postprocessing for materials based on the homogenization method with adaptive finite element methods. Comput Methods Appl Mech Eng 1990;83:143–98.
[34] Benzeggagh ML, Kenane M. Measurement of mixed-mode delamination fracture toughness of unidirectional glass/epoxy composites with mixed-mode bending apparatus. Compos Sci Technol 1996;56:439–49.
[35] Espinosa HD, Dwivedi S, Lu HC. Modeling impact induced delamination of woven fiber reinforced composites with contact/cohesive laws. Comput Methods Appl Mech Eng 2000;183:259–90.
[36] Dharmawan F, Simpson G, Herszberg I, John S. Mixed mode fracture toughness of gfrp composites. Compos Struct 2006;75:328–38.
[37] Krishnan A, Xu LR. An efficient approach to measure the mode ii fracture toughness of materials with preferred interfaces. Int J Fract, submitted for publication.

Please cite this article in press as: Yan H et al. Compression-after-impact response of woven fiber-reinforced composites. Compos Sci Technol (2010), doi:10.1016/j.compscitech.2010.08.012